APPLICATION OF PHYSICS-BASED UNDERWATER ACOUSTIC SIGNAL AND ARRAY-PROCESSING TECHNIQUES TO INFRASOUND SOURCE LOCALIZATION

Gerald D'Spain, Michael Hedlin, John Orcutt, Bill Kuperman,
Catherine deGroot-Hedlin, Lewis Berger, and Galina Rovner

Scripps Institution of Oceanography, University of California, San Diego

Sponsored by Defense Threat Reduction Agency

Contract No. DTRA01-00-C-0061

ABSTRACT

The purpose of this project is to apply physics-based signal and array-processing techniques, recently developed in the area of underwater acoustics, to atmospheric infrasound data and co-located seismic field data. The infrasound data are collected by the eight microbarometers comprising the International Monitoring System (IMS) infrasound station at Pinon Flat (PFO) plus an additional five microbarometer/space filter sensor systems installed for a 6-week period at five Anza seismic station sites located within 40-km range of PFO. The co-located Anza seismic sensors as well as the Incorporated Research Institutes for Seismology (IRIS) seismic station at PFO provide the data needed to perform a comparison between infrasound and seismic recordings of atmospheric events across a very wide horizontal aperture. During the 6-week period, four rocket launches occurred at Vandenberg Air Force Base: an Atlas 2AS, a Taurus, a Titan 4B, and a Delta II. The arriving signals from three of these four launches were recorded with high signal-to-noise ratio. High-quality ground truth information on rocket trajectories and other quantities measured during two of the launches have been acquired from the Vandenberg and Los Angeles Air Force Bases.

OBJECTIVE

The purpose of this project is to apply physics-based signal and array processing techniques, recently developed in the area of underwater acoustics, to atmospheric infrasound data and co-located seismic station field data. The hypothesis to be tested is that advanced underwater acoustic signal and array-processing techniques, with some modifications, can provide more accurate source locations and source signature estimates of low-level events of interest in nuclear explosion and treaty monitoring than conventional methods. In addition, the joint use of infrasonic and seismic data from co-located sensor systems has the potential to significantly increase phase identification and source localization capability, and reduce unwanted background noise.

Basic research questions we are addressing in this project include:

- What are the effects of range-dependent, heterogeneous, and time-variable media on infrasound propagation and source localization?
- How can the location of caustics in infrasound be exploited for source localization? Can the location of these caustics be predicted accurately with available environmental data?
- Can waveguide invariant techniques, which have proven to provide robust and simple approaches to analyses of underwater waveguide propagation, be used effectively with infrasound data?
- What are the important sources of infrasonic noise and signals in the southern California environment? How will these measurements be translated into other areas of the world?
- What acoustic propagation codes (e.g., ones based on a parabolic equation (PE) solution to the acoustic wave equation which includes the effect of winds) incorporate the important propagation physics and so can be used for effective forward modeling in the inverse problems of localizing sources and inferring atmospheric properties?
- A question related to the inverse problem is how effective are sources of opportunity, e.g., mining and quarry blasts, bolides and rocket launches, in calibrating the atmospheric propagation characteristics?
- What are the spatial correlation lengths of various infrasound signals and noise at frequencies of interest scientifically and operationally? How do these correlation lengths vary with topography, weather, humidity, background noise, and other environmental variables?
- How can seismic and acoustic data be used in parallel to understand infrasonic wave excitation and propagation and to localize the source? In particular, how do seismic and acoustic waves couple at the interface between the earth and atmosphere and can this coupling be used to both identify the many wave types observed and infer source location?

The primary goal of this paper is to use high-fidelity numerical modeling methods along with the launch trajectory information and environmental data collected at the time of the launches to determine the predictability of the arrival structure of the signals across the PFO/ANZA array from these 400-km-distant rocket launches. The predictions take into account the signal-distorting effects caused by phase delays across the spatial aperture of the space filters (i.e., each microbarometer/space filter system is not omni-directional over the frequency band of interest). A second goal is to search for any possible phase coherence between the output of a microbarometer and a co-located sonic anemometer.

RESEARCH ACCOMPLISHED

Focused Experiment

A focused infrasound experiment was conducted over the 6-week period from 7 September to 18 October 2001. The 8-element International Monitoring System (IMS) infrasound station (I57US) at the Pinon Flat Observatory (PFO), in the high desert 125 km northeast of San Diego, was the source of much of the data. In addition, data were collected from the co-located, three-component, broadband IRIS (Integrated Research Institutions for Seismology)

seismic station at PFO (an IMS auxiliary seismic station) to permit studies of the relationship between the atmospheric infrasound and seismic wave fields. Fig. 1 shows a map of the 8 I57US microbarometer sensors (H1 thru H4 and L1 thru L4), and the IRIS station, along with a line indicating the back azimuth to Vandenberg Air Force Base. The H-type microbarometers, spaced 100 to 200 m apart, had 18-m rosette space filters attached and the L-type sensors, forming a centered triangle with nominal 1.4-km-long sides, had 70-m diameter space filters. The space filters cause each of the infrasound sensors to become a directional receiver with frequency-dependent characteristics; this issue will be discussed further below.

As part of the focused experiment, a microbarometer/space filter sensor system was installed at each of five Anza seismic station sites located within 40-km range of PFO. The space filters at these stations were composed of 4 porous tubes of 15-m length each, arranged in a "plus" (+) pattern as symmetrically as the layout of each site allowed. Fig. 2 is a map of the topography along with the locations of the 5 Anza stations (RDM, KNW, CRY, WMC, and SND) and PFO. A line indicating the back azimuth to Vandenberg Air Force Base again is included in the figure.

Data from the Titan 4B Launch

During the 6-week focused experiment, four rocket launches were conducted at Vandenberg Air Force Base, 400 km to the west-northwest of PFO. The rockets were an Atlas 2AS, a Taurus, a Titan 4B, and a Delta II. Fig. 3 shows a 10-min time series of the arrivals from the Titan 4B as recorded by all 13 infrasound sensors. The data were band-filtered between 1 and 3 Hz. Time 0 on the plot corresponds to 21:40:00 GMT, 5 October, 2001 (JD 278), which is 19 min after the announced launch time. Assuming that the first arrival was created when the rocket first reached supersonic speed, then it has a group velocity of approximately 300 m/s. The waveforms at each of the stations are dominated by three major arrivals, occurring at 22.5 min, 24 min, and 25.4 min after launch in the uppermost traces. Numerical modeling results discussed below indicate that the first arrival is the stratospheric refracted arrival, the first part of the second arrival is also the stratospheric refracted arrival when the rocket reaches the upper regions of the stratosphere whereas the second part is the refracted arrival from the lower part of the thermosphere, and the third arrival initially reflects from the ground and then refracts from higher altitudes in the thermosphere. Therefore, the spread in arrival structure is associated both with the motion of the rocket through the atmosphere and the propagation characteristics through the stratospheric waveguide.

Variations in arrival structure across the 40-km aperture of the array are clearly visible. In addition, the arrival structure recorded by the sensors with 18-m space filters (the uppermost 4 "I57H" traces) is different than that recorded by the sensors with 70-m filters (the "I57L" traces). The corresponding spectrogram of the time series recorded by the temporary infrasound station at Anza station Red Mountain (IRDM) is presented in Fig. 4. The arrivals from the rocket launch have energy that extends up to 5 Hz. However, this higher frequency energy is strongly attenuated by the 70-m space filters, as discussed below.

White-noise-constrained adaptive plane-wave beam forming (Gramann, 1992; Cox, Zeskind, and Owen, 1987) has been applied to the Titan 4B arrivals. Fig. 5 shows the results of the processing on the second part of the second, main arrival (just after the 5-min mark in the upper traces in Fig. 4) using just the data collected by the 8 I57US sensors. The analysis was done only up to 2.5 Hz to avoid the higher frequencies where the 18-m and 70-m space filters have significantly different response characteristics. The white-noise-constraint value used for the results in the figure is 2.5 dB down from 10*log(N) where N is the number of array elements. (Using a constraint value of 10*log(N) is equivalent to conventional array processing). The two-dimensional (2-)D array frequency/wave number processing output is a function of frequency, time, wave number (or slowness), and azimuth. Fig. 5 presents a plot of frequency vs. wave number at a fixed azimuth of 285 deg, the back azimuth having greatest energy for the second arrival. The slope of the dark ridge of energy in the plot passing through the origin equates to a phase velocity of around 359 m/s. A similar plot for the first arrival indicates a phase velocity of 350 m/s. Both estimates are accurate to within about 5 m/s, so the difference in the two results appears to be significant. This phase velocity difference is consistent with the numerical modeling results where the stratospheric refracted arrival has an apparent phase velocity of around 345 m/s (it depends somewhat upon the altitude of the rocket) and the lower thermospheric refracted signal arrives with nearly a 355 m/s phase velocity.

In addition to searching for differences in the arriving phase velocities of the major arrivals in the time series in Fig. 3, several additional adaptive beam forming calculations were done to look for possible differences in azimuth of arrival. The trajectory of the rocket took it to the southwest from the launch site, so that an evolution in azimuth

might be evident in the data. The results showed that all arrivals had back azimuths within 1 or 2 deg of 285 deg. The second part of the second arrival in Fig. 3, i.e., the energy just after the 5-min mark in the upper traces, may have arrived a degree or two from a more southerly direction than the first part just prior to the 5-min mark, but this difference probably is within the beam former resolution.

Numerical Modeling using CASS/GRAB

The Comprehensive Acoustic System Simulation (CASS) program (Weinberg *et al*, 2001; Weinberg and Keenan, 1996) is being used to perform the numerical modeling. The CASS program, developed at the Naval Undersea Warfare Center, Division Newport, is a US Navy-standard code that has been approved by the Navy's Oceanographic and Atmospheric Master Library (OAML). To obtain OAML accreditation, the code underwent extensive testing and has been thoroughly documented. CASS actually is a modular collection of codes that allow all aspects of sonar system performance to be modeled. One of the acoustic propagation models in CASS is the Gaussian Ray Bundle (GRAB) model (Weinberg and Keenan, 1996), which was used in this work. Gaussian ray bundles and Gaussian beam tracing represent recent advances in ray theoretically based modeling, which provides more accurate wave field amplitude results (Jensen *et al*, 1994; see also Cerveny *et al*, 1982). GRAB allows for range dependence of the sound speed profiles and range dependence in the bottom interface (which is either the ocean bottom in hydroacoustic modeling or the Earth topography in atmospheric infrasound), so that propagation in a 3-D varying medium is done using an N X 2-D approximation.

In addition to its more advanced amplitude modeling capability and extensive testing and documentation, the advantages of using CASS/GRAB are that it includes several options for modeling a variety of physical phenomena, the source code is included with the distribution, and it can easily be run in batch mode. Although CASS/GRAB was developed for the underwater sonar problem, the only significant adaptation required for modeling infrasound propagation in the atmosphere was to place an artificial, flat, pressure release upper boundary at 150-km altitude (i.e., zero "depth"). The program is run to search for eigenrays in the ± 60 deg about horizontal launch angle interval, but no rays are allowed in the solution that interact with the artificial interface at 150 km.

Information on the position of the rocket as a function of time at 1-sec intervals after launch was provided by the personnel at Los Angeles Air Force Base, with valuable assistance from individuals at Vandenberg Air Force Base. According to the trajectory information, the rocket became supersonic 8 sec after launch at an altitude of about 300 m. The numerical modeling starts at this position (see McLaughlin *et al*, 2000) and continues for the 242 sec it takes for the rocket to exceed 150 km in altitude. The results presented here are limited to the 8- to 200-sec interval after launch.

The sound speed profile information used as input to the propagation modeling was derived from data from two sources. First, Douglas Drob at the Naval Research Laboratory provided us with profiles of temperature and the meridional and zonal wind profiles at 1-km increments up to 170-km altitude and at approximately 10-km-spaced points along two great circle paths, from PFO to the rocket launch point and from PFO to the splash down point of one of the jettisoned components. Profiles were provided for two different time periods, 1800 GMT and 2400 GMT, 5 Oct, which bracket the launch time. The modeling presented here uses only the profiles along the great circle path from PFO to the launch position, and only from the 2400 GMT, 5 Oct time period. The second source of sound speed information came from the empirical atmospheric models (the Horizontal Wind Model and the Extended Mass Spectrometer - Incoherent Scatter Radar temperature model) contained in the Infrasonic Modeling of Atmospheric Propagation (InfraMAP) tool kit (Norris *et al*, 1999).

Range-dependent modeling, both range dependence of the sound speed profiles and of the topography over land, has been performed. However, only the range dependence of the topography has been incorporated in the modeling results presented here. Effective range-independent sound speed profiles were obtained by first averaging the temperature, meridional, and zonal wind profiles along the great circle path separately. Then, an effective profile was derived by adding the projection of the horizontal wind vectors along the great circle path to the sound speed profile based on the temperature data alone. The left panel in Fig. 6 shows a comparison of the effective range-averaged sound speed profiles from the Drob data (solid curve) and from InfraMAP (dashed curve). The Drob-derived profile has more structure in the stratospheric waveguide (0-50 km altitude), almost forming two ducts, than the InfraMAP profile. This structure has a strong effect on the predicted signal arrival structure, as discussed below. The right hand panel shows the attenuation profile for a frequency of 1 Hz used in the modeling. This profile was extracted from the InfraMAP output (0 - 120 km) and then extrapolated to 150 km.

A fundamental property of propagation in a waveguide is its dispersive characteristics. By providing a measure of the relationship between the group and phase velocities of the various multi-path components in a wavefield, the waveguide invariant quantifies in a single scalar parameter these dispersive characteristics (e.g., D'Spain *et al*, 2000; D'Spain and Kuperman, 1999). Plots of the invariant ("inverse beta") for the two range-averaged sound speed profiles in Fig. 6 are presented in Fig. 7. Again, the solid curve pertains to the profile obtained from the Doug Drob data and the dotted curve is for the InfraMAP-derived profile. The horizontal line at the invariant value of zero indicates where no dispersion occurs (i.e., a broadband pulse remains a pulse) whereas increasingly larger positive and negative values signify increasing amounts of dispersive spreading (and pulse distortion). Two transitions appear in the curves: between 5.5 and 6 deg and between 13.0 and 13.5 deg in the solid curve. The first transition occurs when the ray angles become sufficiently steep that the lower boundary of the waveguide no longer is created by refraction, but by reflection from the ground. (The receiver altitude is taken to be the 1280-m altitude of PFO). The second transition between 13.0 and 13.5 deg is more relevant to the rocket launch data and occurs when the ray angles become sufficiently great that the energy is no longer trapped in the stratospheric waveguide. The important difference between the solid and dotted curves occurs just prior to this transition. That is, the solid curve shows an asymptotic approach to the horizontal line at zero, whereas the InfraMAP curve crosses over it. The implication of this asymptotic approach is that the dispersion is very small over a fairly wide interval of ray angles, so that focusing of broadband pulse energy will occur (Kuperman *et al*, 2001).

The CASS/GRAB 1-Hz modeling results of the eigenray amplitudes as a function of time after rocket launch for the two sound speed profiles in Fig. 6 are shown in Figs. 8 and 9. The predicted arrival structure for the two cases is remarkably different. Whereas the InfraMAP profile (Fig. 9) yields only two major arrivals with the first arrival being the largest in amplitude and having a duration longer than 2 min, the Drob-derived profile (Fig. 8) predicts a small amplitude first arrival followed by a 1-min gap and then a large-amplitude second arrival. This large-amplitude arrival is the result of the broadband focusing evident from the waveguide invariant plots in Fig. 7(as discussed in the previous paragraph). Both sound speed profiles indicate a short duration arrival at the 25-min mark surrounded by low-level "coda". They also both predict that a gap occurs around the 24 min mark, although it is significantly shorter for the Drob-derived profile than for the InfraMAP profile. A comparison with Fig. 3 shows that the Drob-derived profile results provide a much better match to the main features in the actual measurements. That is, they reproduce the relative amplitudes of the first and second arrivals, the 1-min gap between the first and second arrivals, the short duration nature of the gap at the 24-min mark, and the fact that three or four arrivals are present.

To better identify the components of the arrival structure in the Drob-derived predictions, and in the actual data, the eigenray arrivals are plotted as a function of both time after launch and rocket altitude. (Note that the time scale is from 20 to 34 min after launch rather than 19 to 29 min as in Figs. 8, 9, and 3). This plot represents a rocket trajectory travel-time curve. Two different sizes of dots are used to provide an indication of eigenray amplitude. (Fig. 8 is the result of integrating along each vertical line in Fig. 10). Three different branches are evident in the figure. The first, starting at the 21-min mark, is the stratospheric refracted path, the second is the lower thermospheric refracted arrival, and the third, which bifurcates from the second as the rocket altitude increases, is the path that reflects first from the ground and then refracts from higher altitudes in the thermosphere.

Therefore, the first arrival in Figs. 3 and 8 is the stratospheric refracted path that exists when the rocket is at low altitudes. This path disappears as the rocket passes through the upper troposphere and lower stratosphere because of the small medium sound speeds at these altitudes, leading to the 1-min gap between first and second arrivals. The first part of the second arrival actually is the reappearance of this path as the rocket ascends into the upper stratosphere where medium sound speeds are greater. The received amplitudes at PFO are largest from this portion of the rocket trajectory. The short gap around the 24-min mark is the time separation between the latest arriving stratospheric refracted path energy and the lower thermospheric refracted energy. That is, the arrivals just on either side of the 5-min mark in Fig. 3 represent these two different phases. The trailing energy arriving last has reflected from the ground before refracting in the thermosphere.

Plane Wave Response of Space Filters

Each inlet port of the space filters acts as an omni-directional point receiver. The outputs from each of these receivers are summed together at the microbarometer without any relative phase delay since the distance from each port to the microbarometer is the same. This summation is equivalent to forming a broadband beam in the vertical

direction whose character is determined by the 2D spatial distribution of the ports. (In some deployments, the 3D distribution should be taken into account). The plane wave response of the directional receiver characteristics of a 70-m space filter as a function of frequency and elevation angle are shown in Fig. 11. The incoming plane wave is assumed to have unity amplitude so that its mean squared amplitude is 0.5 (-3 dB). Because of the relative phase delays due to propagation across the horizontal aperture of the space filter, the signal amplitude becomes increasingly attenuated with increasing frequency above 1 Hz at the smaller elevation angles. Complete destructive interference occurs along an arc in the frequency/elevation angle plane starting at 5 Hz and 0 deg elevation angle (horizontal). Similar plots show little variation as a function of azimuth so that the response is effectively isotropic in the horizontal plane. Also, no shift in signal phase occurs due to the space filter response so that only its effects on amplitude need to be taken into account. All of the various issues associated with the distorting effects of the rosette space filters are discussed in Hedlin *et al*, 2002.

(No) Phase Coherence Between Wind Velocity and Infrasonic Wind Noise

A focused experiment was conducted at PFO to examine the coherence between the time series from an MB 2000 microbarometer without a space filter and the three components of wind velocity as measured by a co-located sonic anemometer. The goal was to investigate the possibility of using adaptive noise cancellation processing (Widrow, 1976) to remove wind noise contamination in the microbarometer time series. These types of processing schemes allow the phase correlated component (as measured by coherence) between two time series to be separated from the uncorrelated component. Therefore, if sufficient coherence exists between the anemometer and microbarometer time series, then an anemometer could replace a space filter, thus minimizing land use and saving deployment costs.

A total of 166 hours (nearly 7 days) of continuous data were recorded from 4-11 Mar (JD 063-070) 2002. An MB 2000 was placed at a height of 2 m above ground and adjacent to a sonic anemometer at the same height. All six channels of data - two from the microbarometer and four from the sonic anemometer - were digitized at a 20 samples/sec rate and recorded on the same data acquisition system. Fig. 12 shows a plot of 20 min of time series from the two output channels from the MB 2000 (lower-most two panels with the second-from-bottom trace being the output high-pass filtered above 0.05 Hz) and the four channels of output from the sonic anemometer (upper four panels). Although some similar features can be seen in the time series for the three components of wind velocity (upper-most three traces) and the microbarometer infrasound output (second-from-bottom trace), no statistically significant coherence between the infrasound time series and any wind velocity component time series was found at any frequency at any time over the full 166 hours of the experiment.

CONCLUSIONS AND RECOMMENDATIONS

Infrasound signals with large signal-to-noise ratio were recorded by 13 sensors, including the 8 I57US elements at PFO, during a Titan 4B rocket launch at Vandenberg Air Force Base, 400 km distant. Numerical modeling was performed with the CASS/GRAB program, a US Navy standard Gaussian ray bundle-based code, with rocket trajectory information from Los Angeles Air Force Base. The results using profiles of temperature and horizontal winds provided by Douglas Drob at the Naval Research Laboratory show good agreement with the main features of the measured arrival structure. The first arrival is a stratospheric refracted return when the rocket is at low altitudes, followed by a 1-min gap as the rocket passes through the upper troposphere and lower stratosphere where the medium sound speeds are too small to support this path. However, once the rocket ascends into the upper stratosphere where the sound speeds are greater, this path reappears. Its reappearance is marked by large received amplitudes due to broadband focusing, as predicted by waveguide invariant techniques. A short gap in time follows, terminated by the arrival of lower thermospheric-refracted energy. These arrivals have detectable amplitudes also because of broadband focusing. The signals arriving last traveled paths that reflected from the ground before refracting in the thermosphere at higher altitudes. All these components of the arrival structure are clearly illustrated by a rocket trajectory travel-time curve. White-noise-constrained adaptive beam forming on the first arrival and on the thermospheric-refracted arrival yield phase velocity estimates that differ by 10 m/s, consistent with the difference expected from the numerical modeling results.

The 2-D spatial distribution of the individual ports of the space filters acts like a beam former to point a beam in the vertical direction. Therefore, each microbarometer is converted into a directional receiver. The signal-attenuating effects of this vertical beam must be taken into account at frequencies above 1 Hz for the 70-m filters.

Finally, no statistically significant coherence was found between the infrasound time series from an MB 2000 microbarometer and the three wind velocity components as measured by a co-located sonic anemometer.

ACKNOWLEDGEMENTS

We would like to thank the personnel at Los Angeles and Vandenberg Air Force Bases for their efforts in providing us with the rocket launch data. Anton Dainty of the Defense Threat Reduction Agency assisted in acquiring these data. Special thanks to Doug Drob of the Naval Research Laboratory for sending us the environmental data. Clint Coon and Frank Vernon at Scripps provided assistance in installing the temporary infrasound stations and Clint set up the microbarometer/anemometer experiment. In addition, Ruth Keenan of SAIC and Dave Ensberg at Scripps provided help with running the CASS/GRAB code.

Finally, we want to extend a warm thank you to the landowners who allowed us to install our sensors and porous hoses on their land.

REFERENCES

Cerveny, V., M. M. Popov, and I. Psencik (1982), Computation of Wave Fields in Inhomogeneous Media - Gaussian Beam Approach, Geophys. *J. R. Astr. Soc*., **70**, 109-128.

Cox, H., R. M. Zeskind, and M. M. Owen (1987), Robust Adaptive Beamforming, IEEE Transactions of Acoustics, Speech and Signal Processing ASSP-35 (10).

D'Spain, G. L., W. A. Kuperman, J. A. Orcutt, and M. A. H. Hedlin (2000), Long-Range Localization of Impulsive Sources in the Atmosphere and Ocean from Focus Regions in Single Element Spectrograms, Proc. of 22nd Annual Seismic Research Symposium: Technol. for Monitoring the Comprehensive Nuclear-Test-Ban Treaty, 8 pgs.

D'Spain, G. L. and W. A. Kuperman (1999), Application of Waveguide Invariants to Analysis of Spectrograms from Shallow Water Environments that Vary in Range and Azimuth*, J. Acoust. Soc. Am*., **106** (5), 2454-2468.

Gramann, R. A. (1992), ABF Algorithms Implemented at ARL-UT, ARL Tech. Letter ARL-TL-EV-92-31, Applied Research Laboratories, The University of Texas at Austin, Austin, TX.

Hedlin, M. A. H., B. Alcovarro, and G. L. D'Spain (2002), Evaluation of Rosette Infrasonic Noise-Reducing Spatial Filters, submitted to *J. Acoust. Soc. Am*., 28 pgs.

Jensen, F. B., W. A. Kuperman, M. B. Porter, and H. Schmidt (1994), *Computational Ocean Acoustics*. American Inst. Physics, New York, 168-170.

Kuperman, W. A., G. L. D'Spain, and K. D. Heaney (2001), Long Range Source Localization from Single Hydrophone Spectrograms, *J. Acoust. Soc. Am*.,**109** (5) pt. 1, 1935-1943.

McLaughlin, K. L., A. Gault, and D. J. Brown (2000), Infrasound Detection of Rocket Launches, Proc. of 22nd Annual Seismic Research Symposium: Technol. for Monitoring the Comprehensive Nuclear-Test-Ban Treaty, 219-230.

Norris, D., R. Nadel, and R. Gibson (1999), User's Guide for InfraMAP, v. 1.4, BBN Tech. Memo. W1353a, BBN Technologies, Arlington, VA.

Weinberg, H., R. L. Deavenport, E. H. McCarthy, and C. M. Anderson (2001), Comprehensive Acoustic System Simulator (CASS) Reference Guide, NUWC-NPT TM 01-016, Naval Undersea Warfare Center Division Newport, RI.

Weinberg, H. and R. E. Keenan (1996), Gaussian Ray Bundles for Modeling High-Frequency Propagation Loss under Shallow-Water Conditions, *J. Acoust. Soc. Am*., **100** (3), 1421-1431.

Widrow, B., J. M. McCool, M. G. Larimore, and C. R. Johnson (1976), Stationary and Nonstationary Learning Characteristics of the LMS Adaptive Filter, *Proc. IEEE*, **64** (8), 1151-1162.

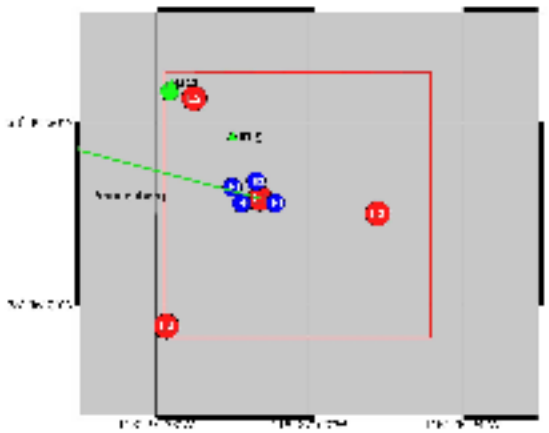

Figure 1. Map of the I57US infrasound station at Pinon Flat Observatory (PFO).

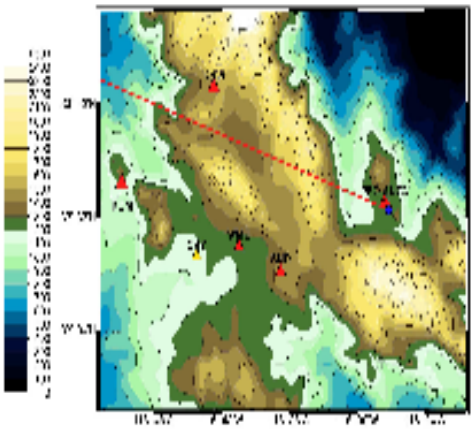

Figure 2. Map of PFO and the five ANZA stations where infrasound sensors were temporary installed for the focused experiment, along with the surrounding topography

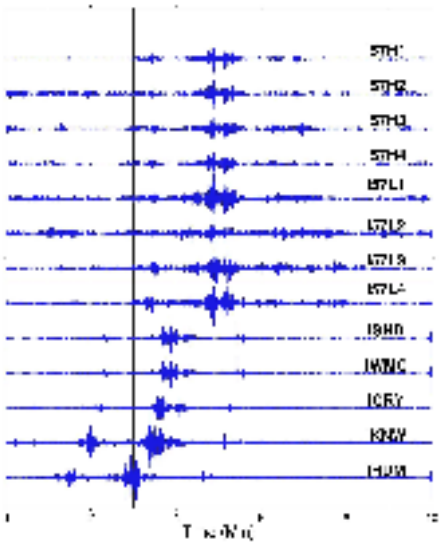

Figure 3. Time series of arrivals from the Titan 4B launch recorded by all 13 infrasound sensors, band-pass filtered from 1 to 3 Hz.

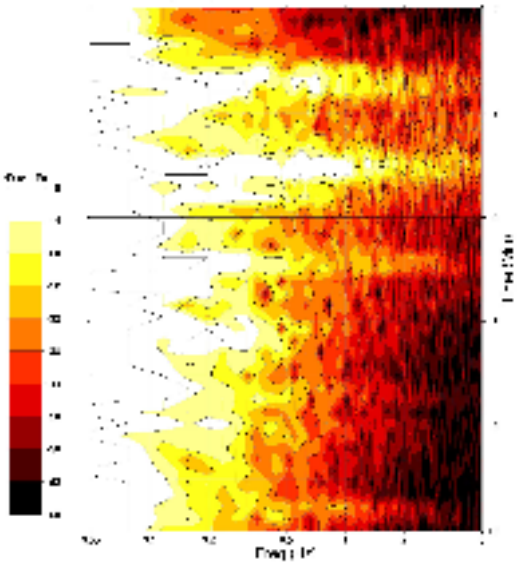

Figure 4. Spectrogram of data recorded by station IRDM over the same 10-min period as Fig. 3 (lower-most trace).

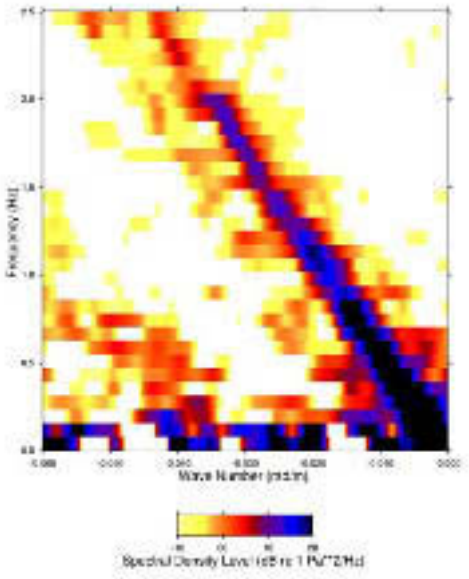

Figure 5. White-noise-constrained adaptive beam forming on the 2nd part of the 2nd (main) arrival from the Titan 4B launch at 285 deg back azimuth.

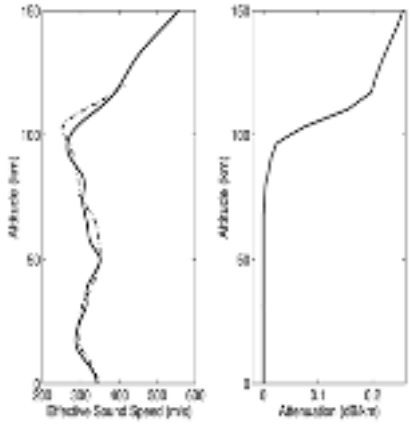

Figure 6. Effective range-averaged sound speed profiles (left panel) derived from NRL data (solid curve) and from InfraMAP databases (dashed curve), and the attenuation profile at 1 Hz (right panel) used in the modeling.

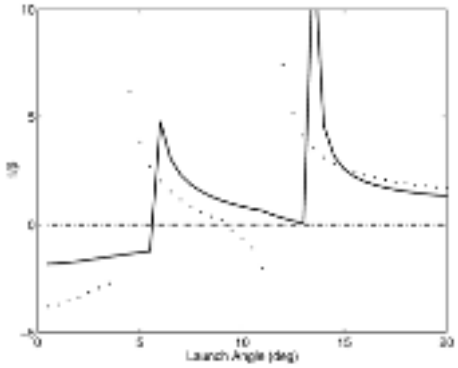

Figure 7. The waveguide invariant as a function of arrival angle for the two sound speed profiles in Fig. 6 and for an altitude corresponding to I57US.

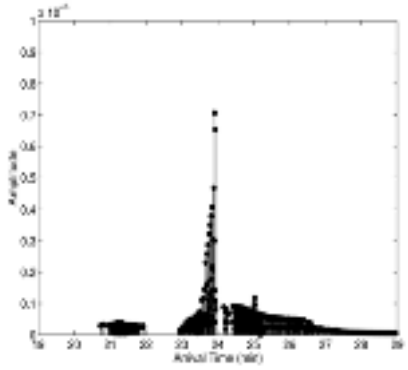

Figure 8. The amplitude vs. arrival time at PFO of the CASS/GRAB eigenrays created in the 8- to 200-sec time interval by the Titan 4B rocket modeled as a moving point source for the NRL-data-derived sound speed profile (solid curve in Fig. 6).

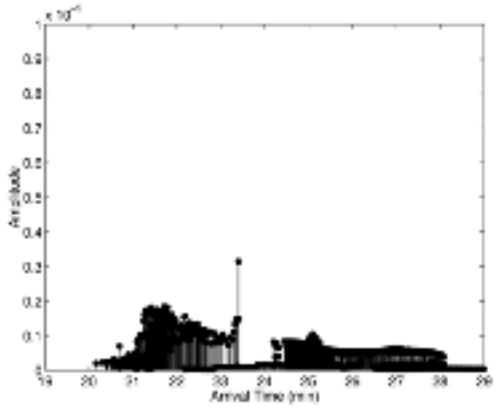

Figure 9. CASS/GRAB-modeled eigenray amplitude vs. arrival time at PFO for the InfraMAP-derived sound speed profile (dashed curve in Fig. 6).

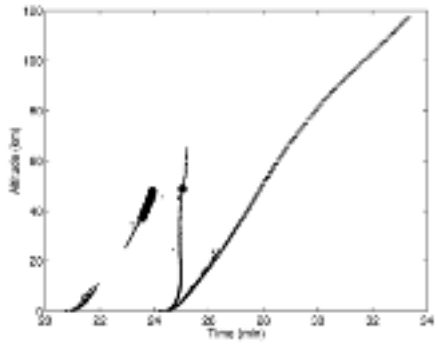

Figure 10. The CASS/GRAB-modeled eigenray arrival times at PFO as a function of rocket altitude. The large and small circles signify eigenray amplitudes greater or less than 1.0 x 10-6, respectively.

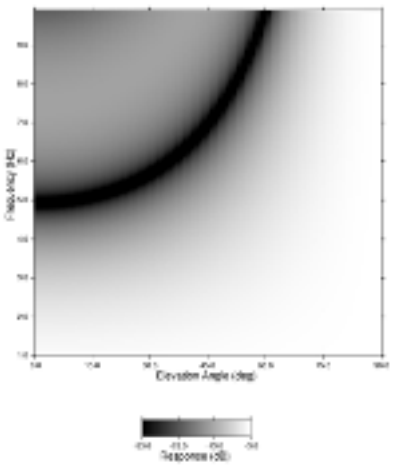

Figure 11. Plane wave response of the 70-m rosette space filters as a function of frequency and elevation angle of arrival.

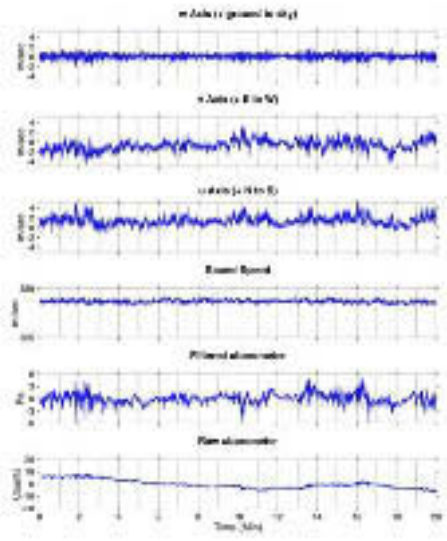

Figure 12. 20-min time series of the 4 output channels of a sonic anemometer (3 components of wind velocity, and sound speed, respectively) and the 2 channels of a co-located microbarometer.